AO17: Detecting sulphur dioxide emissions from volcanoes with the Cross-track Infrared Sounder

Candidate number: 1043995
Supervisors: Dr I. A. Taylor, Dr R. G. Grainger

April 2023

Abstract

Gaseous emissions from volcanoes can present hazards, including to aviation safety and the environment. In this project, a fast detection method for sulphur dioxide (SO_2) gas from volcanoes, developed by Walker et al. (2011) for use with the Infrared Atmospheric Sounding Interferometer (IASI) satellite instrument, is extended to the Cross-track Infrared Sounder (CrIS) instrument. The method uses statistics of an ensemble of spectra measured over background SO_2 levels to minimise the effect of noise. It is applied using CrIS to the 2021 eruption of La Soufrière, St Vincent, and results are compared with those from IASI. The two implementations are found to agree for this case study, demonstrating CrIS's potential for near real-time hazard detection. Some discrepancies between them are found: these likely emerge from different choices of background ensemble, which in turn affect the variance of the results.

1 Introduction

Measurement of volcanic gas emissions is an important tool for assessing volcanic hazards and the study of underlying volcanic processes. The three most prevalent gases released from volcanoes are water vapour, carbon dioxide, and sulphur dioxide (SO_2) (Symonds et al., 1994). Having the lowest climatological background, SO_2 is the most commonly monitored of these for volcanological purposes.

Emissions of gas and ash from volcanoes pose several hazards. Firstly, aircraft flying through plumes may be damaged by high concentrations of sulphuric acid aerosols formed from SO_2 (Prata, 2009), and by fine ash, which can be collocated with SO_2 soon after eruptions (Hyman and Pavolonis, 2020). Many human health risks are also associated with exposure to elevated levels of SO_2 (Thomas and Watson, 2010). Furthermore, SO_2 in the weather system can lead to acid rain, impacting ecological systems, while SO_2 injected into the stratosphere forms aerosols which cause significant global cooling (Thomas and Watson, 2010).

In addition to hazard detection, monitoring of volcanic gas emissions over time can be used to study volcanoes' intrinsic behaviour. Changing rates of emission may indicate subsurface volcanic activity, which can signal an impending eruption (Sparks, 2003).

Satellites have been used for remote sensing of volcanic SO_2 emissions since 1982 (Krueger, 1983), and useful satellite data stretches as far back as 1978 (Carn et al., 2016). Remote sensing of SO_2 has historically been performed using ultraviolet (UV) radiation (Hyman and Pavolonis, 2020), as there are strong absorption features of the SO_2 molecule in this spectral region. However, the molecule also absorbs in the mid-infrared, and this has been exploited for detecting SO_2 in recent decades. The UV method measures the contribution of atmospheric SO_2 to back-scattering of solar radiation. Conversely, the infrared technique quantifies the contrast in thermal radiation between emissions from the surface and from SO_2 at higher altitudes. Gas at altitude will absorb up-welling radiation with frequencies within its absorption band, which is then re-emitted with lower radiance due to its colder temperature, following the Planck function. The infrared technique consequently has the advantage of working in absence of sunlight, for example at night-time or in high latitude winters, allowing more frequent coverage than offered by UV measurements. This project employs the infrared technique.

The so-called ν_1 and ν_3 absorption features ("symmetric" and "asymmetric stretch", centred at $1152\,\mathrm{cm}^{-1}$ and $1362\,\mathrm{cm}^{-1}$ respectively) of SO_2 both lie in the thermal infrared region. The ν_1 band is in a spectral region free of interfering atmospheric species but is the weaker of these features. The ν_3 band, meanwhile, overlaps with broad absorption of water vapour, limiting detection sensitivity in the moist lower troposphere. Despite the reduced sensitivity at lower altitude, the stronger ν_3 feature is used for detection in this project, as it offers a clear signal at heights relevant to the most hazardous volcanic eruptions.

Satellite remote sensing is a valuable tool for volcanic gas detection. Ground-based detection is often

limited by local factors such as geography, politics, and safety. Sparks et al. (2012) note that most active volcanoes have little to no specialised monitoring, including a significant number deemed to pose a high risk to large populations. Satellite measurements, which allow global coverage, circumvent these issues of poor local monitoring.

Instruments on satellites in polar orbits can scan, with few gaps, the entire Earth's surface twice daily. The Cross-track Infrared Sounder (CrIS) instrument is mounted on satellites in such an orbit. It is a Fourier-transform spectrometer that records broad infrared spectra at each of its pixels. These measure 14 km in diameter when observing at nadir. The instrument flies on the NASA/NOAA (National Oceanic and Atmospheric Administration) collaboration Joint Polar Satellite System (JPSS) satellites, of which there are three in orbit at time of writing (SNPP and NOAA-20 operational, and NOAA-21 undergoing verification). Successful detection of SO_2 using CrIS has already been demonstrated, albeit using a more sophisticated method than presented here, by Hyman and Pavolonis (2020).

Instrument	**CrIS**	**IASI**
Swath width	2200 km	2200 km
Pixel size at nadir	14 km	12 km
Average sampling distance	16 km	24 km
Spectral resolution	0.625 cm^{-1}	0.5 cm^{-1}
Equatorial crossing time (ascending)	13:30	21:30
Number in orbit	3	2
Further planned launches	2027, 2032	none

Table 1: Comparison of CrIS and IASI instruments.

The CrIS instrument is similar to the Infrared Atmospheric Sounding Interferometer (IASI) which is on-board the two Meteorological Operational (MetOp) satellites currently flying, developed by ESA and operated by EUMETSAT (European Organisation for the Exploitation of Meteorological Satellites). A third MetOp satellite was de-orbited in November 2021 after reaching the end of its operational lifespan. The SO_2 detection method implemented in this project was developed for the IASI instrument and has been used successfully for over a decade (Walker et al., 2011). Details of the two instruments are shown in table 1. Noise characteristics of the instruments are similar in the spectral region of interest. The Walker et al. (2011) method is expected to also be successful when applied using CrIS due to CrIS and IASI's similarities. With a smaller sampling distance, CrIS takes over twice as many measurements within the same scanning area. Furthermore, the crossing times—which are at a fixed local solar time due to the satellites' Sun-synchronous orbits—are different, with CrIS instruments following 4 hours after IASI. CrIS can therefore complement IASI by doubling daily coverage and reducing the maximum gap between measurements from 12 to 8 hours.

2 Methods

The method used in this project—which will be referred to as the "linear retrieval"—follows the "ensemble method" laid out by Walker et al. (2011). A retrieval refers to inference of atmospheric properties using remote measurements. In the ensemble method, a matrix operator is built from observed statistical parameters and theoretical predictions. When applied to the spectrum measured at a pixel, it yields an estimate of the column density of SO_2 in the atmosphere at that pixel.

2.1 Elements of the retrieval

In the ensemble approach, variability in the background is characterised by the statistics of a large sample of real measured spectra, free of volcanic SO_2. The N background spectra, denoted $\mathbf{y}_j \in \mathbb{R}^n$, are combined into a mean spectrum $\bar{\mathbf{y}}$ and covariance matrix $\mathbf{S}_{\boldsymbol{\epsilon}}$:

$$\bar{\mathbf{y}} = \frac{1}{N}\sum_{j=1}^{N}\mathbf{y}_j,\ \mathbf{S}_{\boldsymbol{\epsilon}} = \frac{1}{N-1}\sum_{j=1}^{N}(\mathbf{y}_j - \bar{\mathbf{y}})(\mathbf{y}_j - \bar{\mathbf{y}})^T.$$

The spectral band chosen includes all channels with wavenumbers between 1300 cm^{-1} and 1410 cm^{-1} to incorporate the SO_2 ν_3 absorption feature centred at 1362 cm^{-1}. Generating the covariance with real measured spectra avoids the need for detailed quantification and propagation of individual error sources; rather, the covariance accounts for the total variability in SO_2-free spectra. This includes sources of both statistical uncertainty such as instrument noise and systematic uncertainty such as viewing angle. Meanwhile, it represents a general atmospheric state with no prior knowledge of parameters such as its temperature profile and the presence of meteorological cloud or trace gases. Such simplicity makes the retrieval computationally efficient.

The theoretical prediction is calculated using a radiative transfer model, in this case the Reference Forward Model (RFM, Dudhia, 2017). The model

is used to calculate a Jacobian $\mathbf{k} \in \mathbb{R}^n$ defined as $k_i = \frac{\partial y_i}{\partial x}(x_0)$, with y_i the brightness temperature measured in the i^{th} CrIS channel, x the total SO_2 column density in Dobson units (DU), and x_0 its climatological average. The Jacobian thus specifies the expected change in brightness temperature measured by each CrIS channel in the presence of SO_2.

2.2 Retrieval calculation

Having calculated the mean spectrum $\bar{\mathbf{y}}$, covariance matrix $\mathbf{S}_{\boldsymbol{\epsilon}}$, and Jacobian $\mathbf{k}$, the optimal retrieval estimate for SO_2 column density $\hat{x}$ at a CrIS pixel is given by (see Rodgers, 2000, section 4.1):

$$\hat{x} = x_0 + (\mathbf{k}^{\mathrm{T}}\mathbf{S}_{\boldsymbol{\epsilon}}^{-1}\mathbf{k})^{-1}\ \mathbf{k}^{\mathrm{T}}\mathbf{S}_{\boldsymbol{\epsilon}}^{-1}(\mathbf{y} - \bar{\mathbf{y}}) \qquad (1)$$

where x_0 is the climatological SO_2 column density of the chosen profile of the RFM, and $\mathbf{y}$ is the spectrum measured at the pixel to evaluate, in units of brightness temperature. The total retrieval error uncertainty is given by:

$$\hat{\sigma}_x = (\mathbf{k}^{\mathrm{T}}\mathbf{S}_{\boldsymbol{\epsilon}}^{-1}\mathbf{k})^{-\frac{1}{2}}. \qquad (2)$$

This is the least squares solution including error. It assumes that measurements follow a linear model of the form $\mathbf{y} = \mathbf{k}x + \boldsymbol{\epsilon}$, with the total measurement error $\boldsymbol{\epsilon}$ normally distributed with covariance $\mathbf{S}_{\boldsymbol{\epsilon}}$. It is also assumed for this retrieval that there is no prior information of x. The technique has been applied successfully for detection of SO_2, in both the infrared using IASI (Walker et al., 2011, 2012), and in the UV with the Tropospheric Monitoring Instrument (TROPOMI, Theys et al., 2021).

The method's simplicity can be demonstrated as follows. Since the Jacobian is a vector in this case, the pre-factor $(\mathbf{k}^{\mathrm{T}}\mathbf{S}_{\boldsymbol{\epsilon}}^{-1}\mathbf{k})^{-1}$ in equation 1 is a normalising scalar. The vector $\mathbf{k}^{\mathrm{T}}\mathbf{S}_{\boldsymbol{\epsilon}}^{-1}$ gives the error-weighted contribution of each spectral channel to the total SO_2 level, such that its dot product with the spectral offset $\mathbf{y} - \bar{\mathbf{y}}$ yields the total SO_2 column density above background.

The linear retrieval method has only two controlling factors. Firstly, the background profile of SO_2 and temperature (as a function of height) used in the forward model determines the Jacobian $\mathbf{k}$ and climatological background column density x_0. Secondly, the choice of spectra used in the background ensemble fixes $\mathbf{S}_{\boldsymbol{\epsilon}}$ and $\bar{\mathbf{y}}$. An ensemble should be large enough to represent the full variability of the background; though as the ensemble grows, the retrieval error increases due to the ensemble encompassing a more varied background (Walker et al., 2011).

The column density $\hat{x}$ derived from equation 1 should be treated only as a qualitative indicator of presence of SO_2. This is because the detected value depends strongly on the assumed height (and temperature profile) of SO_2 when calculating the Jacobian $\mathbf{k}$. The recorded brightness temperature offset for a fixed amount of SO_2 increases with its thermal contrast with the surface, and so this type of retrieval is more sensitive to SO_2 at atmospheric cold points, principally the tropopause (Walker et al., 2012). The method is further limited by the assumption of a linear response to SO_2. Given the complexity of the radiative transfer processes involved, this assumption will not always hold, and for very large quantities of SO_2, absorption features may saturate.

The linear retrieval technique improves upon the brightness temperature difference (BTD) method which has commonly been implemented as a detection filter, such as by Clarisse et al. (2008). A BTD filter detects SO_2 by comparing a pair of spectral regions, one within an absorption band of SO_2 and one free from the effects of SO_2 absorption. Including many spectral channels in the linear retrieval minimises the effect of noise, hence it is shown to be more sensitive than a BTD approach by up to an order of magnitude (Walker et al., 2011). It is computationally faster than a more detailed retrieval, which may use an iterative process to achieve fully quantitative results (see e.g. Carboni et al., 2012). Further, the linear retrieval can be used in tandem with such a retrieval to flag pixels where an iterative retrieval should be performed (Taylor et al., 2018, 2022).

For the linear retrieval, a detection threshold can be defined such that if $\hat{x}$ lies above it, the pixel is "flagged" to contain SO_2. The background distribution of $\hat{x}$ is assumed normal with mean x_0 and standard deviation $\hat{\sigma}_x$. Next, a Z-score (number of standard deviations from the mean) is chosen to give the required level of significance. A positive detection is registered when:

$$\hat{x} > x_0 + Z_{\text{thresh}}\hat{\sigma}_x. \qquad (3)$$

2.3 Data processing

2.3.1 Pre-processing

The processing routine for the CrIS linear retrieval begins with raw spectra in radiance units. These are then apodised: this is an operation which corrects for effects caused by the finite path difference sampled in the Fourier transform spectrometer. The spectra are then converted to units of brightness temperature, at which point they are ready to be used to form the background statistics as detailed in section 2.1, or to have the linear retrieval applied.

2.3.2 Implementing the retrieval

Following from equation 1, the *gain operator* $\mathbf{g} \in \mathbb{R}^n$ is defined as follows:

$$\mathbf{g} = (\mathbf{k}^{\mathrm{T}}\mathbf{S}_{\boldsymbol{\epsilon}}^{-1}\mathbf{k})^{-1}\ \mathbf{k}^{\mathrm{T}}\mathbf{S}_{\boldsymbol{\epsilon}}^{-1},$$

allowing the expression for $\hat{x}$ to be recast as:

$$\hat{x} = x_0 + \mathbf{g} \cdot (\mathbf{y} - \bar{\mathbf{y}}),$$

with $x_0 = 0.1097\,\mathrm{DU}$ the background SO_2 column density used in the RFM to evaluate the Jacobian. In practice, this operation is carried out on many spectra at once. Defining a matrix $\mathbf{Y}' \in \mathbb{R}^{n\times m}$ of m spectra whose columns are the spectral offsets from background $(\mathbf{y} - \bar{\mathbf{y}})$, the SO_2 column densities $\hat{\mathbf{x}} \in \mathbb{R}^m$ for m pixels are retrieved as:

$$\hat{\mathbf{x}} = x_0\mathbf{1}_m + \mathbf{Y}'^{\mathrm{T}}\mathbf{g},$$

with $\mathbf{1}_m = (1, 1, ..., 1)^{\mathrm{T}} \in \mathbb{R}^m$ a vector of ones. Executing this matrix product avoids the use of typically slow 'for' loops in Python, in which the retrieval was coded. The operation is thus computationally fast, allowing near real-time application of the retrieval.

2.3.3 Post-processing

If midnight UTC occurs while the CrIS or IASI instruments scan the plume, the changing longitude of their orbits will cause adjacent plume data to appear to be split between days. This splitting can result in artefacts due to measurements displayed side-by-side being taken about 24 h apart. To fix this, the times of pixels flagged to contain SO_2 were plotted on histograms separately for ascending and descending satellite passes (where the satellite is travelling towards and away from the North Pole, respectively), which revealed clear peaks where SO_2 was detected. A time offset for loading daily measurements of each pass, effectively converting to an approximate local time, was then estimated so that the data from each peak was processed and displayed in chronological order.

To make a fair baseline for comparison between CrIS and IASI data, retrieved SO_2 column densities were averaged over cells in a $0.5^\circ \times 0.5^\circ$ grid for each instrument type. The threshold chosen in equation 3 could then be applied to grid squares to flag those where SO_2 has been observed. The total error in the average column density $\bar{x}$ calculated at each cell combines the retrieval error $\hat{\sigma}_x$ with the standard deviation σ_{s} of the M pixels within the cell:

$$\sigma_{\bar{x}} = \sqrt{(\hat{\sigma}_x^2 + \sigma_{\mathrm{s}}^2)/M}. \tag{4}$$

Appendix A.1 describes the derivation of this formula. The measured plume area was found to be convergent for grid spacing above 0.3°; this resolution ensures that each cell will contain at least one measurement. The error in individual cells decreased with larger grid spacing due to the higher pixel count M within each square, but with an associated loss in spatial resolution. The grid square size was chosen as a compromise between resolving plume features and reducing error.

2.4 Calculation of ensemble statistics

The background ensemble formed for the CrIS linear retrieval comprised all valid CrIS spectra within the rectangular region bounded by 42° N, 0° E, 5° N, and 72° W, between 25$^{\mathrm{th}}$ March and 30$^{\mathrm{th}}$ April 2020. This amounted to some 4.5 million spectra in total. Care was taken to ensure that no volcanic sources of SO_2 were included in this dataset. The region contains the La Soufrière volcano and the date range is one year before its eruption (see section 3.1). It is therefore expected that the ensemble captures the variability of SO_2-free spectra sufficiently well for the region and season of interest.

Data from the two active CrIS instruments were aggregated separately. Retrieval errors calculated from equation 2 are:

$$\begin{aligned} \hat{\sigma}_x^{\text{SNPP}} &= 0.7405\,\mathrm{DU}, \\ \hat{\sigma}_x^{\text{NOAA-20}} &= 0.5045\,\mathrm{DU}. \end{aligned} \tag{5}$$

The SNPP CrIS instrument has a notably larger retrieval error than the NOAA-20 instrument. This may be in part due to cumulative damage sustained over SNPP's longer mission, having spent 6 more years in space than NOAA-20. Additionally, during the SNPP CrIS instrument's validation, it was found that one of the sensors in its 3×3 scanning array has a noise level significantly higher than others and above specification (CrIS SDR Team, 2018); this higher noise may contribute to the difference between error estimates in equation 5.

Grid-averaged CrIS retrievals, as described in section 2.3.3, incorporate both SNPP and NOAA-20 CrIS instruments, so the retrieval errors were averaged for application to the grid statistics. The detection threshold for CrIS was calculated with equation 3 setting $Z_{\mathrm{thresh}} = 1.960$, such that 97.5% of background readings should lie below it. This threshold retains most true signal while excluding most of the background. The IASI threshold was taken from Walker et al. (2012), where a much stricter Z-score of $Z_{\mathrm{thresh}} = 5.199$ was used, excluding all but one part in 10 million of the background. The resulting

thresholds are:

$$x_{\text{thresh}}^{\text{CrIS}} = 1.3095\,\text{DU},$$
$$x_{\text{thresh}}^{\text{IASI}} = 0.4909\,\text{DU}. \quad (6)$$

Importantly, the background ensemble evaluated to implement the IASI linear retrieval is different to CrIS's. Walker et al. (2012) used 196 042 spectra from April 2009 measured over a region bounded by 70° N, 10° E, 30° N, and 40° W when building their covariance. A matching ensemble cannot be replicated with CrIS data as the first such instrument began operation in 2012, so the ensemble statistics are not expected to match.

3 Results and discussion

3.1 The 2021 eruption of La Soufrière

The case study selected to test and validate the retrieval was the 2021 eruption of La Soufrière, on the island of Saint Vincent, in Saint Vincent and the Grenadines. An effusive eruption, comprising slow release of gas and magma, started in December 2020, before explosive eruptions began at 08:41 local time (12:41 UTC) on 9$^{\text{th}}$ April 2021. Frequent explosions continued until 12$^{\text{th}}$ April, releasing large plumes of ash and gas which reached altitudes of ~ 20 km (Yue et al., 2022). After this, the frequency and strength of eruptions dwindled substantially until ceasing altogether on 22$^{\text{nd}}$ April. The event forced the evacuation of nearly 20 000 people, and copious deposition of ash damaged some buildings (Global Volcanism Program, 2021).

The retrieval method was applied to spectra measured by the two CrIS instruments after the eruption. Results for column density at each pixel were then grid-averaged as described in section 2.3.3. The gridding procedure was also applied to linear retrieval results from the three IASI instruments (from Taylor et al., 2022) which were operational at the time of the eruption. Figures 1 and 4 (see appendix A.2) contain maps of the results for eight days after the explosive eruption began. It should be noted that subsequent plots in the same column are spaced 12 hours apart, and the data in IASI plots are recorded approximately 8 hours after the data for the adjacent CrIS plot (local time 1.30am/pm for CrIS vs 9.30am/pm for IASI).

Figure 1 shows that CrIS clearly detects the SO_2 plume's growth and dispersal in the days after the explosive phase begins. SO_2 is already detected on the CrIS instruments' ascending passes on 9$^{\text{th}}$ April (top left) at 17:02 UTC, less than 5 hours after the first explosion. Up to 12$^{\text{th}}$ April, high levels of SO_2 are observed; this corresponds with the date that SO_2 emission rates begin to decrease (Taylor et al., 2022). By this time, the plume has spread ~ 5000 km to the east across the Atlantic Ocean, reaching Africa's west coast. Slower southward and westward motion is also visible over the South American continent, with the plume tracing out the varying wind directions across the region.

From 13$^{\text{th}}$ April, a strong signal is seen above Ecuador; this is a plume from the country's Sangay volcano (2.00° S, 78.34° W). This eruptive event was registered contemporaneously by seismic monitoring and satellite data (Global Volcanism Program, 2021a). Meanwhile, some weaker signal is detected from the Sabancaya volcano in Peru (15.79° S, 71.86° W), where explosions and emissions of gas and ash were also reported in this period (Global Volcanism Program, 2021b). These detections show potential for using the CrIS linear retrieval to monitor SO_2 from smaller eruptions.

As the plume from La Soufrière continues to evolve in figure 4 (see appendix A.2), primarily in the eastward direction, its column density reduces due to the SO_2 being advected, diffused, and removed through atmospheric chemical processes with timescales on the order of days (Carn et al., 2016). The meandering of the plume as it travels eastwards is a result of the SO_2 being carried by the northern hemisphere subtropical jet stream. As it travels, it traces out atmospheric Rossby waves within the jet stream.

3.2 Comparison of results from CrIS and IASI

With the retrieval results for the two instruments displayed side-by-side in figures 1 and 4, one can qualitatively compare the two. Agreement is generally strong; both the plume's overall shape and detailed variations in its density evolve sensibly between the instruments' results. There are, however, distinct differences between the two. The retrieval with IASI is more sensitive to areas of low SO_2 concentration (see how the edges of the plume vary), while the retrieval using CrIS is more likely to measure very high values of effective SO_2 column density within the plume.

These effects are illustrated in figure 2. Figure 2(a) contains histograms of grid-averaged SO_2 column densities detected by CrIS and IASI in a complete scan of the plume during the daytime of 12$^{\text{th}}$ April. Figure 2(b) contains SO_2 detection profiles of the same plume scan as a function of longitude, for a fixed latitude of 3.75° N. It should be noted that

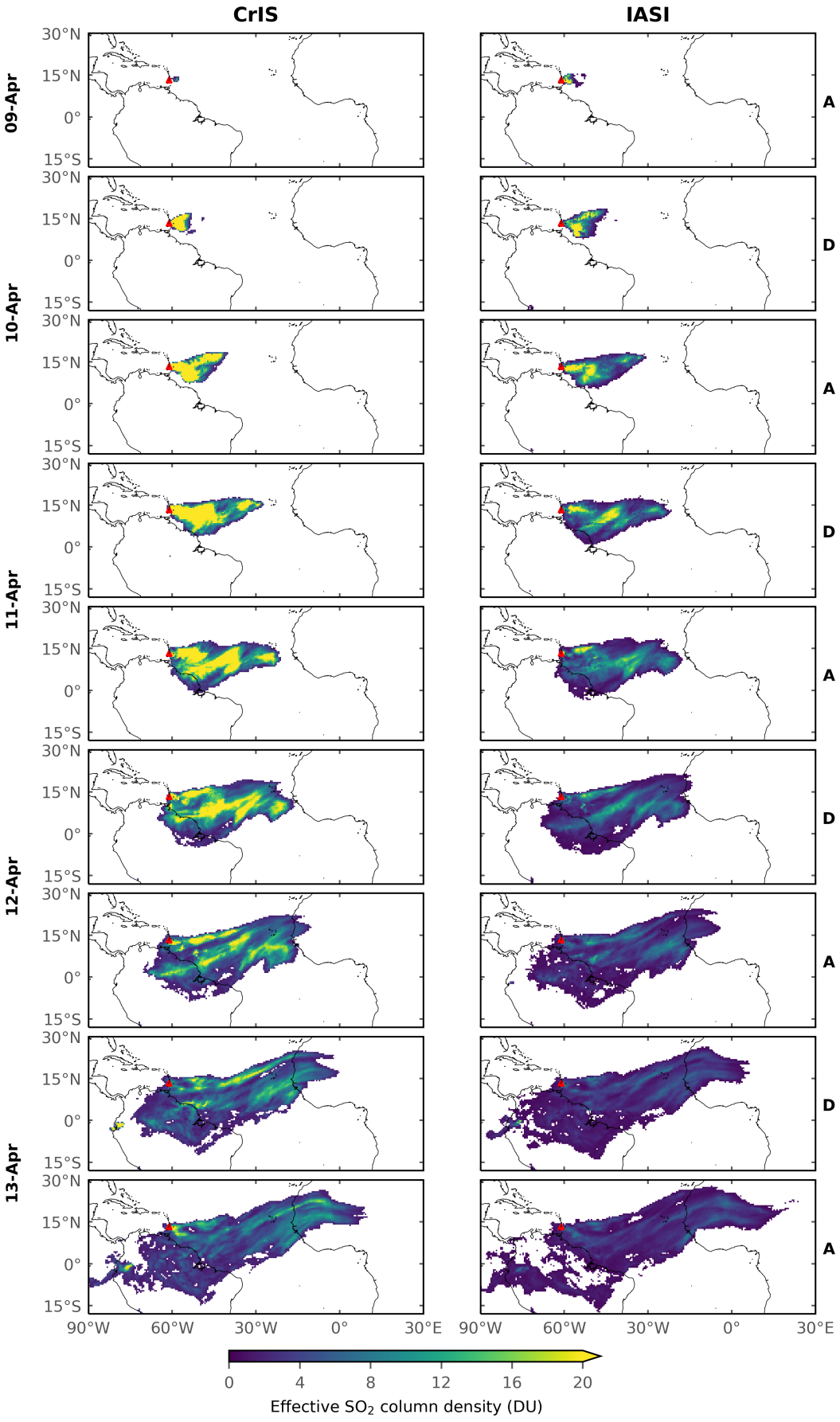

Figure 1: Maps showing grid-averaged linear retrieval of SO_2 observing the April 2021 eruption of La Soufrière. The maps contain estimated column densities from CrIS (left) and IASI (right), plotting only values above each instrument's detection threshold. The red triangle marks the volcano's location. The labels **A** and **D** on the right-hand side denote rows with readings from ascending and descending passes. Discrepancies between the two instruments are largely attributed to the effects of different background ensembles used. Continued in appendix A.2, figure 4.

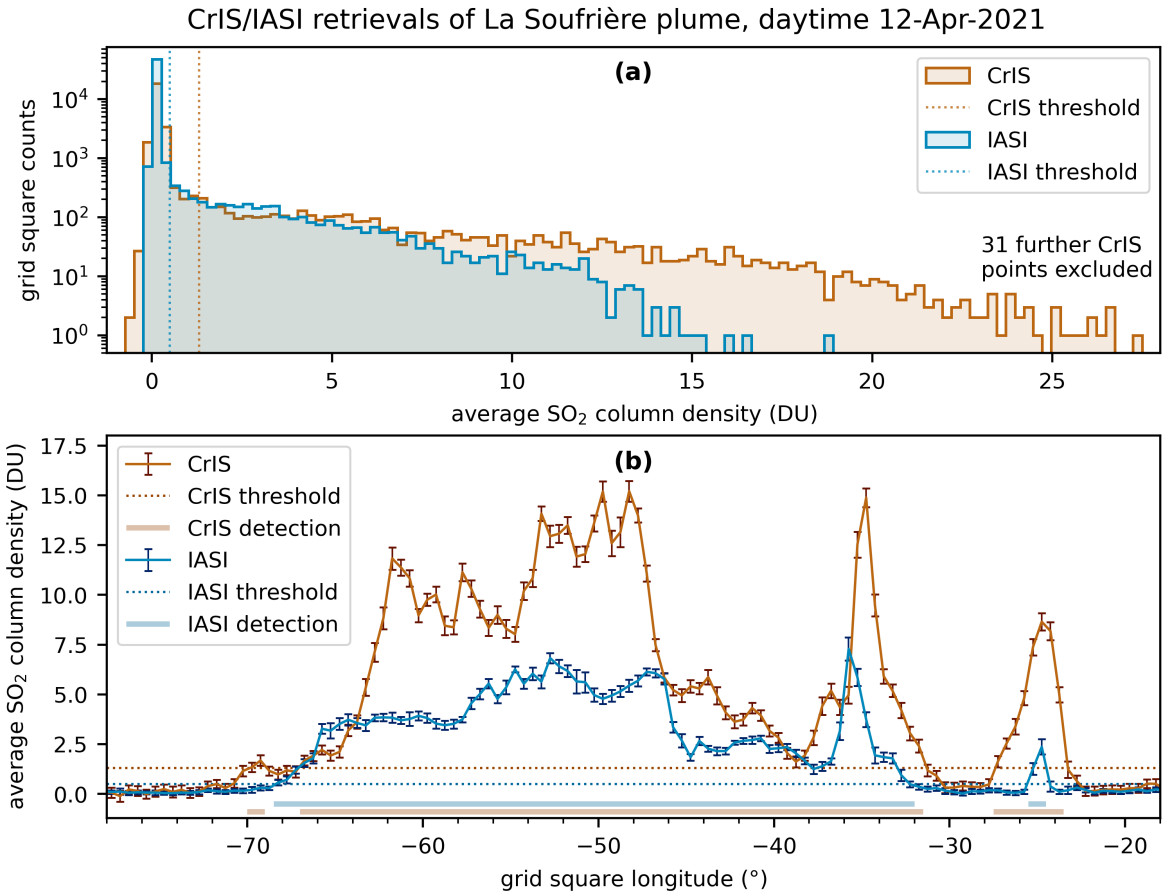

Figure 2: Comparisons of linear retrievals for CrIS and IASI at the La Soufrière eruption. Data are taken from daytime overpasses on 12th April, with the CrIS measurements lagging those of IASI by about 4 hours. **(a):** Histograms of grid-averaged SO_2 values for the instruments. Note for CrIS the wider background spread (~ 0 DU) and higher frequency of large values. **(b):** Plume density profile at a latitude of 3.75° N for CrIS and IASI. The regions of detection (solid horizontal lines at the bottom) largely overlap between the instruments, with some discrepancies.

due to the different equatorial crossing times of the two instruments, the CrIS measurements lag those of IASI by about 4 hours.

From the histograms in figure 2(a), the differences between the spread in observations by CrIS and IASI can be readily seen. The width of the peak due to background is wider for CrIS than IASI (note that the y-axis is logarithmic), including a substantially larger number of CrIS grid squares with average column densities < 0 DU. On the other end, CrIS detects far more grid cells with large column densities; indeed, 31 cells were found to have values that lie above the 28 DU maximum of the histogram.

The plume cross-sections shown in figure 2(b) show further complexity in the variation between the two implementations of the retrieval. Effects of the 4 h time difference between the two instruments' readings are evident, as the eastern edge of the plume moves slightly east in the time from IASI's until CrIS's measurements (see for example the peak around 35° W). When SO_2 is detected, the column density measured by CrIS is, for the most part, considerably larger, matching the statistics summarised in figure (a). This difference is sometimes less distinct (e.g. around 66° W). There is good agreement in regions of no detection, though at the edges of the plot the greater background variability of CrIS is perceptible. Comparison of the thick horizontal lines (indicating positive detection) to the solid curves demonstrates how the flagged region of the plume varies between instruments. They disagree in some places (such as around 25° W), but in others CrIS's higher threshold compensates for its greater retrieved values and its flagged region matches IASI's as expected (32° W).

The error in the CrIS linear retrieval, averaged between the SNPP and NOAA-20 instruments, is $\hat{\sigma}_x^{\mathrm{CrIS}} = 0.6225$ DU. For IASI, the retrieval error was much lower at $\hat{\sigma}_x^{\mathrm{IASI}} = 0.0776$ DU. These uncertainties led to the threshold values in equation 6, where

it is seen the CrIS threshold is more than twice as high as that of IASI. The CrIS detection threshold is necessarily higher due to its larger retrieval error, and so the CrIS linear retrieval is not able to detect SO_2 as reliably as the IASI linear retrieval in regions of low concentration.

Such a large discrepancy between the CrIS and IASI retrieval errors is most likely a result of the different background ensembles used to create the two retrievals. CrIS's ensemble incorporates over 20 times more spectra than that of IASI; these spectra are also taken from a wider spatial and temporal range, and the two ensembles cover different regions. Consequently, the CrIS ensemble almost certainly includes more variability than that of IASI, hence the CrIS linear retrieval is expected to have a larger error. The higher spectral resolution of IASI (sampling at $0.5\,\mathrm{cm}^{-1}$ vs $0.625\,\mathrm{cm}^{-1}$ for CrIS, see table 1) could also contribute to the discrepancy between errors. The IASI retrieval then has 1.25 times as many channels within the wavenumber range examined; this extra information could help to reduce the effect of noise on IASI retrievals, reducing their error.

The inconsistency in detecting higher levels of SO_2 may indicate a systematic issue in evaluating the Jacobian. A standard profile for the USA atmosphere with a climatological SO_2 column density of $x_0 = 0.1097\,\mathrm{DU}$ was used to calculate the Jacobian $\mathbf{k}$ for the CrIS retrieval. The IASI retrieval used a profile with a lower value of $x_0 = 0.076\,\mathrm{DU}$ (Walker et al., 2011). Two distinct values of x_0 linearise the model in different regions of phase space. Any difference in the resulting $\mathbf{k}$ vectors will then lead to a discrepancy between retrievals, whose magnitude is greatest far from the linearisation point x_0. Hence when the true column density x is large, the inconsistency between CrIS and IASI retrievals is highlighted. Further, the non-linearity of the real system makes relating the two linear retrievals difficult—this is evident in the complex relationship between the retrievals in figure 2(b). It is also possible that the increased variability in the CrIS background ensemble has a non-trivial magnifying effect via its covariance matrix $\mathbf{S}_{\boldsymbol{\epsilon}}$.

3.3 Measurements of the plume area

To further investigate the retrieval implemented with CrIS, the total area of flagged grid squares was calculated. A plot comparing this with the same results for IASI is shown in figure 3. The area was calculated by summing the areas of grid cells with SO_2 amounts above the detection threshold. Error bounds were then computed as the area of the plume when increasing or decreasing each square's average column density by its error as calculated in equation 4. The plot shows very good agreement between retrievals with CrIS and IASI for the first four days after the eruption begins.

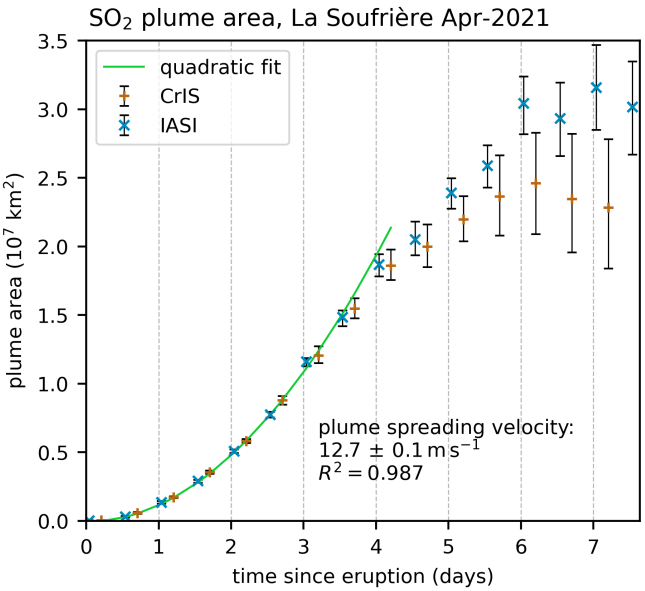

Figure 3: Area of the La Soufrière SO_2 plume over time, evaluated by summing the area of grid cells with mean column densities above the relevant detection threshold. Expansion for the first 4 days is approximately quadratic with time. Later, the results of CrIS and IASI diverge, as the CrIS retrieval is less sensitive to thinning SO_2.

Four days after the eruption, the trends of the two begin to diverge, with CrIS detecting a systematically lower area of SO_2. This observation is borne out by the map plots (figures 1 and 4). After this much time in the atmosphere, the density of SO_2 is decreasing due to advective spreading, diffusion, and chemical processes. As a result, the true column densities are lower, and so the differing retrieval sensitivities for low SO_2 have a significant impact on the measured plume area. With a larger error, the CrIS retrieval has a higher threshold that excludes areas of the plume where there is only a thin layer of SO_2, thus detecting a plume of smaller area. In any case, the sparseness of the plume's extremities at this stage in its life means that its area is not very well defined. Error in the area is high for both instruments due to many cells' retrieved column densities lying around the threshold values.

In figure 3, the initial period of agreement between the two instruments appears to evolve quadratically with time. To test this agreement, the first 18 area measurements were fitted to a quadratic form. The coefficient of the t^2 term has dimensions of a velocity squared, so it was posed that the area $A(t) = \tilde{v}^2 t^2$. The speed $\tilde{v}$ represents a characteristic speed at which the plume spreads horizontally. The

least-squares regression used for the fit found a value of $\tilde{v} = (12.7 \pm 0.1)\,\mathrm{m\,s^{-1}}$, with reported uncertainty resulting from the regression algorithm. The fitted curve is plotted in figure 3.

Comparing against data from Taylor et al. (2022), the characteristic speed $\tilde{v}$ is found to match the average wind speed at the volcano from 9$^{\text{th}}$ to 22$^{\text{nd}}$ April, at an altitude of both 10 km and 16 km. Over this period, the wind at these levels is blowing most often to the ESE; this is the direction of the plume's travel early in figure 1. Data from Taylor et al. (2022) show further that 16 km is approximately the height where the largest density of SO_2 is detected in their quantitative SO_2 retrieval using IASI, which retrieves a profile of the gas as a function of height.

There is good agreement between the measured average wind velocity at the plume's densest altitude and its characteristic spreading speed inferred in this project with dimensional analysis. This consistency suggests that $\tilde{v}$ could be related to kinematic properties of the plume, such as its motion by advection or diffusion. Further analysis of other eruptions could probe whether their SO_2 plumes also follow a quadratic growth pattern.

4 Conclusions

The fast SO_2 detection method developed by Walker et al. (2011) for the IASI instrument has been successfully extended to the CrIS instrument in this project, and good overall agreement was found between the two. Notwithstanding the differing sensitivities of the two implementations, believed to arise from different choices of background spectra, this result demonstrates CrIS's capacity to detect SO_2 from volcanoes.

In particular, the project has highlighted the potential of using CrIS for reliable near real-time detection of volcanic hazards to aviation. Starting with unapodised radiance data, it takes on average 1.8 s to analyse a "granule" of pixels recorded over 6 minutes, containing over 12 000 spectra. Near real-time detection with the linear retrieval is thus limited only by the speed of data transfer from the satellite, via NOAA processing, to the machine where the retrieval is implemented. This can be a 3–6-hour delay, but it is likely lower for operational centres. As a result, it is anticipated that the CrIS linear retrieval could broaden the operational detection suites of organisations monitoring volcanic hazards.

Combining readings from both CrIS and IASI allows at least four daily observations (2 from each satellite constellation) with a maximum 8-hour gap. This is a significant improvement upon the two observations with a regular 12-hour gap afforded by either instrument on its own, increasing the temporal resolution of volcanic hazard detection using hyperspectral infrared measurements. Furthermore, the JPSS programme is scheduled to continue (with updated instruments, launching in 2027 and 2032) well into the 2030s. As such, CrIS linear retrieval data will be able to complement similar data from IASI, as well as from its new, improved version (IASI-NG), set to begin launching on board the MetOp-SG satellites in 2025.

A key area to explore and document in order to improve the linear retrieval technique is the effect of diverse choices of background ensemble on the results of the final retrieval. In their SO_2 retrieval with CrIS, Hyman and Pavolonis (2020) calculated background statistics seasonally and regionally in a $5° \times 5°$ grid. A similar approach could improve upon the accuracy of the linear retrieval discussed here, for both CrIS and IASI. However, given that the retrieval is already limited to a qualitative nature due to prior assumptions about the plume's height (see discussion in section 2.2), this may offer only marginal improvements in accuracy. Instead, a single study could compare background ensembles of different sizes, comprising data from different seasons and spatial regions. This could determine whether there is an optimum sample size, and to what extent the geography of the detection region must be well represented by the background ensemble for reliable, low-noise detections.

Beyond the technical details of the retrieval method, the CrIS linear retrieval could be used further to study SO_2 emissions from volcanoes. Analysing volcanic eruptions of different scales, such as the powerful explosion of Hunga Tonga-Hunga Ha'apai in January 2022, or the frequent small eruptive events of Sicily's Mount Etna, may provide deeper understanding of the strengths and weaknesses of the retrieval. Inter-eruptive volcanic degassing could be studied by averaging retrieved results over an extended period, as done with IASI's linear retrieval by Taylor et al. (2018).

Long-term averaging could also be used to investigate and identify large anthropogenic sources of SO_2. Minimising the noise of the CrIS retrieval would likely be needed before attempting this, though averaging over a sufficiently long period may help to reduce noise to acceptable levels.

Finally, the quadratic growth of plume areas discussed in section 3.3 could be investigated. If plumes from other eruptions exhibit the same behaviour as that of La Soufrière, it could be worthwhile to fur-

ther probe the dynamics of the plumes to see if a simple relationship characterising the spreading of SO_2 from volcanoes can be deduced.

References

Carboni, E., Grainger, R. G., Walker, J. C., Dudhia, A., and Siddans, R. A new scheme for sulphur dioxide retrieval from IASI measurements: application to the Eyjafjallajokull eruption of April and May 2010. *Atmospheric Chemistry and Physics*, 12, 2012. ISSN 1680-7316.

Carn, S. A., Clarisse, L., and Prata, A. J. Multi-decadal satellite measurements of global volcanic degassing. *Journal of Volcanology and Geothermal Research*, 311: 99–134, 2016. ISSN 0377-0273.

Clarisse, L., Coheur, P. F., Prata, A. J., Hurtmans, D., et al. Tracking and quantifying volcanic SO2 with IASI, the September 2007 eruption at Jebel at Tair. *Atmospheric Chemistry and Physics*, 8(24):7723–7734, 2008. ISSN 1680-7316.

CrIS SDR Team. Validated maturity science review for NOAA-20 CrIS SDR. Technical report, NOAA Center for Satellite Applications and Research (STAR), 2018. URL `https://www.star.nesdis.noaa.gov/jpss/documents/AMM/N20/CrIS_SDR_Validated.pdf`. Last access 13 March 2023.

Dudhia, A. The Reference Forward Model (RFM). *Journal of Quantitative Spectroscopy and Radiative Transfer*, 186:243–253, 2017. ISSN 0022-4073.

Global Volcanism Program. Report on Soufrière St. Vincent (Saint Vincent and the Grenadines) (Bennis, K.L., and Venzke, E., eds.). *Bulletin of the Global Volcanism Network*, 46:5. Smithsonian Institution, 2021. doi: 10.5479/si.GVP.BGVN202105-360150.

Global Volcanism Program. Report on Sangay (Ecuador) in: Sennert, S. K. (ed.), Weekly volcanic activity report, 14 April–20 April 2021. Technical report, Smithsonian Institution and US Geological Survey, 2021a. URL `https://volcano.si.edu/showreport.cfm?wvar=GVP.WVAR20210414-352090`. Last access 19 March 2023.

Global Volcanism Program. Report on Sabancaya (Peru) in: Sennert, S. K. (ed.), Weekly volcanic activity report, 14 April–20 April 2021. Technical report, Smithsonian Institution and US Geological Survey, 2021b. URL `https://volcano.si.edu/showreport.cfm?wvar=GVP.WVAR20210414-354006`. Last access 19 March 2023.

Hyman, D. M. and Pavolonis, M. J. Probabilistic retrieval of volcanic SO2 layer height and partial column density using the Cross-track infrared sounder (CrIS). *Atmospheric Measurement Techniques*, 13(11): 5891–5921, 2020. ISSN 1867-8548.

Krueger, A. J. Sighting of El Chichón sulfur dioxide clouds with the Nimbus 7 Total ozone mapping spectrometer. *Science*, 220(4604):1377–1379, 1983.

Prata, A. J. Satellite detection of hazardous volcanic clouds and the risk to global air traffic. *Natural Hazards (Dordrecht)*, 51(2):303–324, 2009. ISSN 1573-0840.

Rodgers, C. D. *Inverse methods for atmospheric sounding: theory and practice*. Series on atmospheric, oceanic and planetary physics; v. 2. World Scientific, Singapore; London, 2000. ISBN 9789810227401.

Sparks, R. S. J. Forecasting volcanic eruptions. *Earth and Planetary Science Letters*, 210(1):1–15, 2003. ISSN 0012-821X.

Sparks, R. S. J., Biggs, J., and Neuberg, J. W. Monitoring volcanoes. *Science*, 335(6074):1310–1311, 2012.

Symonds, R. B., Rose, W. I., Bluth, G. J. S., and Gerlach, T. M. Volcanic gas studies - methods, results, and applications. *Reviews in Mineralogy*, 30:1–66, 1994. ISSN 0275-0279.

Taylor, I. A., Preston, J., Carboni, E., Mather, T., et al. Exploring the utility of IASI for monitoring volcanic SO2 emissions. *Journal of Geophysical Research: Atmospheres*, 123, 2018. ISSN 2169-8996.

Taylor, I. A., Grainger, R. G., Prata, A. T., Proud, S. R., et al. Satellite measurements of plumes from the 2021 eruption of La Soufrière, St Vincent (preprint). *Atmospheric Chemistry and Physics Discussions*, 2022:1–33, 2022. doi: 10.5194/acp-2022-772.

Theys, N., Fioletov, V., Li, C., De Smedt, I., et al. A sulfur dioxide Covariance-Based Retrieval Algorithm (COBRA): application to TROPOMI reveals new emission sources. *Atmospheric Chemistry and Physics*, 21 (22):16727–16744, 2021.

Thomas, H. E. and Watson, I. M. Observations of volcanic emissions from space: current and future perspectives. *Natural Hazards (Dordrecht)*, 54(2):323–354, 2010. ISSN 1573-0840.

Walker, J. C., Dudhia, A., and Carboni, E. An effective method for the detection of trace species demonstrated using the MetOp Infrared Atmospheric Sounding Interferometer. *Atmospheric Measurement Techniques*, 4 (8):1567–1580, 2011.

Walker, J. C., Carboni, E., Dudhia, A., and Grainger, R. G. Improved detection of sulphur dioxide in volcanic plumes using satellite-based hyperspectral infrared measurements: Application to the Eyjafjallajökull 2010 eruption. *Journal of Geophysical Research: Atmospheres*, 117(D20), 2012.

Yue, J., Miller, S. D., Straka, W. C., Noh, Y., et al. La Soufriere volcanic eruptions launched gravity waves into space. *Geophysical Research Letters*, 49(8):n/a, 2022. ISSN 0094-8276.

A Appendices

A.1 Calculation of grid cell error

The average column density $\bar{x}$ for a grid cell containing M pixels with retrieved values x_i is:

$$\bar{x} = \frac{1}{M} \sum_{i=1}^{M} x_i.$$

Each x_i has a retrieval error $\hat{\sigma}_x$, so by summing errors in quadrature the retrieval contributes an error $\hat{\sigma}_x/\sqrt{M}$ to $\bar{x}$. Further uncertainty in $\bar{x}$ results from averaging over a spread of values x_i within a cell, and is quantified by the unbiased sample variance:

$$\sigma_s^2 = \frac{1}{M-1} \sum_{i=1}^{M} (x_i - \bar{x})^2.$$

The standard error of the mean is given by $\sigma_s/\sqrt{M}$. Adding the retrieval error $\hat{\sigma}_x/\sqrt{M}$ and averaging error $\sigma_s/\sqrt{M}$ in quadrature yields equation 4.

A.2 Figure

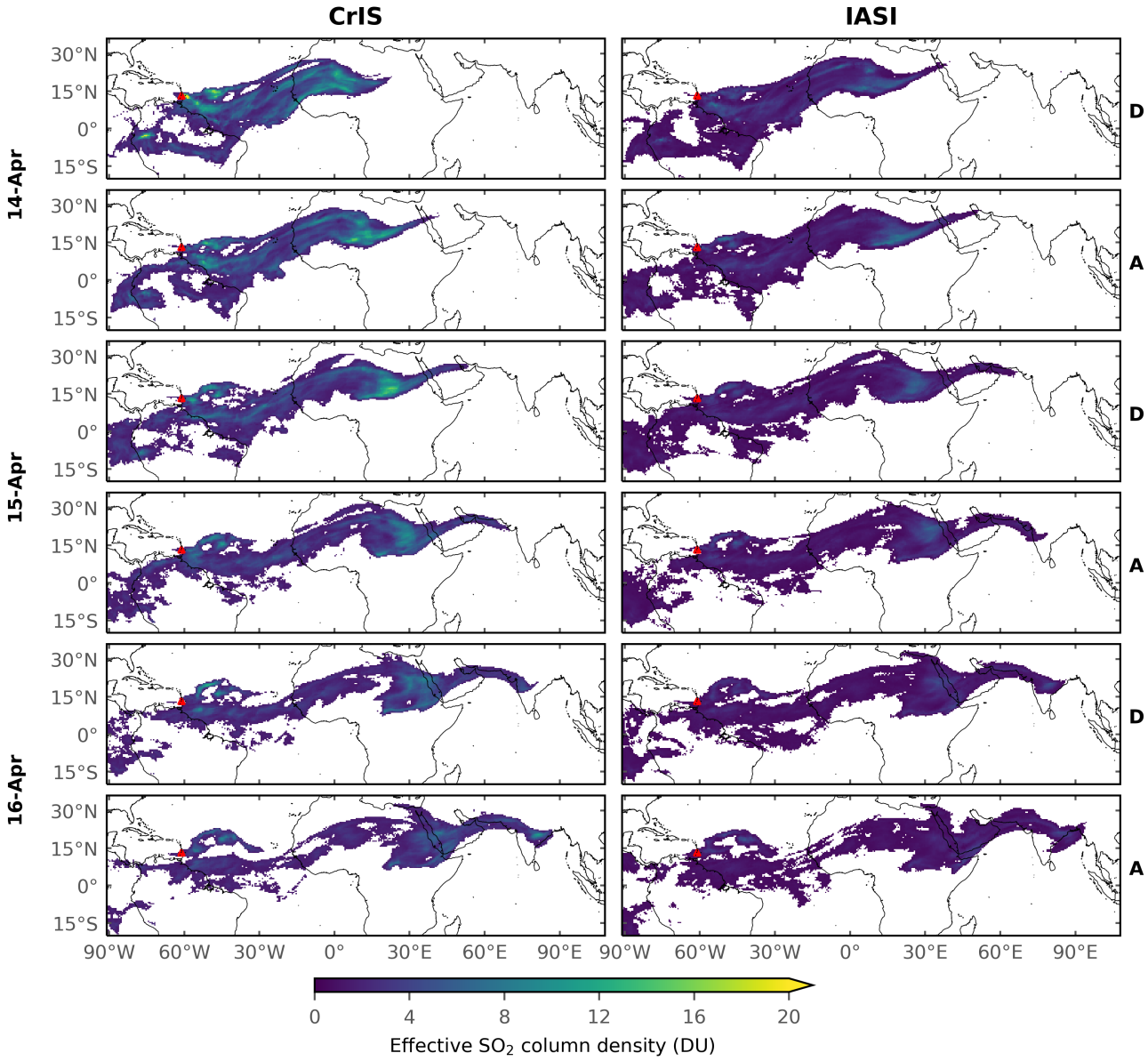

Figure 4: Continuation of figure 1 with an expanded view. Maps show grid-averaged linear retrieval results observing SO_2 from the April 2021 eruption of La Soufrière. The maps contain estimated column densities from CrIS (left) and IASI (right), plotting only values above each instrument's detection threshold. The labels **A** and **D** on the right-hand side denote rows with readings from ascending and descending passes. The plume's shape here highlights Rossby waves in the subtropical jet stream.